



## **Substrate stiffness heterogeneities disrupt endothelial barrier integrity in a micropillar model of heterogeneous vascular stiffening**

Journal:	<i>Integrative Biology</i>
Manuscript ID	IB-ART-07-2018-000124.R1
Article Type:	Paper
Date Submitted by the Author:	07-Oct-2018
Complete List of Authors:	VanderBurgh, Jacob; Cornell University, Biomedical Engineering; Vanderbilt University, Biomedical Engineering Hotchkiss, Halie; Cornell University, Potharazu, Archit; Vanderbilt University, Biomedical Engineering Taufalele, Paul; Vanderbilt University, Biomedical Engineering Reinhart-King, Cynthia; Vanderbilt University, Biomedical Engineering

**Substrate stiffness heterogeneities disrupt endothelial barrier integrity in a micropillar model of heterogeneous vascular stiffening**

**Jacob A. VanderBurgh,<sup>1,2</sup> Halie Hotchkiss,<sup>1</sup> Archit Potharazu,<sup>2</sup> Paul V. Taufalele,<sup>2</sup>**

**Cynthia A. Reinhart-King<sup>1,2,¶</sup>**

**<sup>1</sup> Meinig School of Biomedical Engineering, Cornell University, Ithaca, NY**

**<sup>2</sup> Department of Biomedical Engineering, Vanderbilt University, Nashville, TN**

**¶To whom correspondence should be addressed:**

**Cynthia A. Reinhart-King, PhD**

PMB 351631

Nashville, TN 37235

[cynthia.reinhart-king@vanderbilt.edu](mailto:cynthia.reinhart-king@vanderbilt.edu)

## Abstract

Intimal stiffening has been linked with increased vascular permeability and leukocyte transmigration, hallmarks of atherosclerosis. However, recent evidence indicates age-related intimal stiffening is not uniform but rather characterized by increased point-to-point heterogeneity in subendothelial matrix stiffness, the impact of which is much less understood. To investigate the impact of spatially heterogeneous matrix rigidity on endothelial monolayer integrity, we develop a micropillar model to introduce closely-spaced, step-changes in substrate rigidity and compare endothelial monolayer phenotype to rigidity-matched, uniformly stiff and compliant substrates. We found equivalent disruption of adherens junctions within monolayers on step-rigidity and uniformly stiff substrates relative to uniformly compliant substrates. Similarly, monolayers cultured on step-rigidity substrates exhibited equivalent percentages of leukocyte transmigration to monolayers on rigidity-matched, uniformly stiff substrates. Adherens junction tension and focal adhesion density, but not size, increased within monolayers on step-rigidity and uniformly stiff substrates compared to more compliant substrates suggesting that elevated tension is disrupting adherens junction integrity. Leukocyte transmigration frequency and time, focal adhesion size, and focal adhesion density did not differ between stiff and compliant sub-regions of step-rigidity substrates. Overall, our results suggest that endothelial monolayers exposed to mechanically heterogeneous substrates adopt the phenotype associated with the stiffer matrix, indicating that spatial heterogeneities in intimal stiffness observed with age could disrupt endothelial barrier integrity and contribute to atherogenesis.

## Novelty of the work (20 words max)

We are first to show endothelial monolayers simultaneously contacting stiff and compliant matrix adopt the phenotype associated with stiffer matrix.

## Insight, innovation, integration

Intimal stiffening naturally occurs with age, disrupts endothelial barrier integrity, and contributes to atherosclerosis progression. However, recent evidence has indicated that intimal stiffening is heterogeneous, and it is unclear how the endothelium responds to spatially heterogeneous matrix rigidity. In this study, we developed an *in vitro* micropillar platform to investigate the impact of subcellular scale matrix stiffness heterogeneity on endothelial monolayer phenotype. This approach enabled us to discover that endothelial cells within a monolayer exposed to heterogeneous matrix rigidity adopt the phenotype associated with the stiffest matrix encountered. This suggests subcellular scale spatial heterogeneities in intimal stiffness observed during aging could locally disrupt endothelial barrier integrity and contribute to atherogenesis.

## Introduction

Extracellular matrix stiffening is a hallmark of multiple diseases, including cancer and cardiovascular diseases, and elevated tissue stiffness drives their pathology by altering cellular behavior.<sup>1,2</sup> Vascular stiffening occurs during aging due to changes in the extracellular matrix microarchitecture, and clinically, vascular stiffness is an independent predictor of cardiovascular risk.<sup>3-7</sup> Clinical measures of bulk vascular stiffness mainly reflect medial extracellular matrix remodeling such as collagen deposition or elastin degradation and do not capture intimal mechanics which regulate the ability of the vascular endothelium to form a semi-permeable barrier against circulating lipids and leukocytes.<sup>8</sup> Notably, intimal stiffening as a result of aging or poor diet upregulates endothelial cell contractility, disrupts endothelial adherens junctions necessary for barrier integrity, and ultimately drives endothelial permeability and leukocyte transmigration, hallmarks of atherosclerosis.<sup>2,9-13</sup>

Recent evidence indicates intimal stiffening is accompanied with greater spatial heterogeneity in intimal stiffness.<sup>14</sup> Spatial mapping of aged murine intima with atomic force microscopy force mapping demonstrated that intimal stiffening is characterized by greater point-to-point heterogeneity with subcellular-sized ‘hotspots’ of increased rigidity. Endothelial cells probe the rigidity of their underlying matrix with discrete, force-sensitive focal adhesions.<sup>15–18</sup> Furthermore, single endothelial cells positioned on an interface of stiff and compliant matrix exhibit increased focal adhesion size within the cell body positioned over stiff matrix, demonstrating the ability of single cells to spatially integrate complex mechanical cues.<sup>19</sup> Similarly, single human mesenchymal stem cells positioned over a rigidity interface develop stronger traction forces on the rigid side.<sup>20</sup> However, endothelial monolayers represent an integrated network in which the cytoskeleton of adjacent cells is connected via adherens junctions that act as force mechanotransducers.<sup>15,21–23</sup> Thus, it is unclear how endothelial monolayers integrate complex and conflicting mechanical cues from spatially heterogeneous matrix stiffness.

Here, we designed and implemented a micropillar model of heterogeneous vascular stiffening to investigate how endothelial monolayers integrate complex mechanical cues. Micropillars provide a platform to geometrically control substrate rigidity in a precise manner without changing the cross-sectional area or ligand density available for cell adhesion.<sup>24–26</sup> Furthermore, micropillars enable introduction of large disparities in matrix rigidity without changing surface topography as observed in other platforms that are capable of introducing spatial heterogeneity in substrate stiffness.<sup>19,27–29</sup> As such, we fabricated micropillars with closely spaced, subcellular scale stiffness heterogeneities through incorporation of step-changes in pillar base height. We designed the spacing of our matrix stiffness interfaces such that each endothelial cell within the monolayer would contact stiff and compliant sub-regions to mimic recently reported sub-cellular sized spatial heterogeneities in intimal stiffness while stiffness values were tuned to physiologically relevant rigidities.<sup>14</sup> Our data indicate that endothelial monolayers respond to the stiff ‘sub-regions’ of step-rigidity micropillar arrays preferentially. Adherens junctions on step-rigidity substrates were disrupted equivalently to uniformly stiff substrates relative to uniformly compliant substrates. Similarly, endothelial monolayers cultured on step-rigidity substrates promoted equal leukocyte transmigration percentages to endothelial monolayers on rigidity-matched, uniformly stiff substrates. Interestingly, vinculin recruitment to adherens junctions, leukocyte transmigration frequency, transmigration time, focal adhesion size, and focal adhesion density was equivalent between the stiff and compliant sub-regions of step-rigidity substrates. These findings suggest that endothelial monolayers adopt the phenotype associated with the stiffest matrix they encounter indicating that ‘hotspots’ of increased intimal stiffness observed with age-related intimal stiffening could disrupt endothelial barrier integrity and contribute to atherogenesis.

## **Materials and methods**

### *Fabrication of PDMS micropillar arrays*

Silicon (Si) masters of polydimethylsiloxane (PDMS) micropillar arrays with step-rigidities were etched into Si wafers in a two-step process.<sup>20</sup> Briefly, thin photoresist (SPR220-3.0; Shipley Company, LLC, Marlborough, MA) was spun and patterned with an i-line 5X reduction step-and-repeat projection stepper (AutoStep 200; Integrated Solutions, INC, Twerksbury, MA). Deep reactive ion etching (DRIE) utilizing the Bosch fluorine process was subsequently performed to yield an array of cylindrical holes of uniform depth (Unaxis 770 Deep Si Etcher; Plasma-Therm, LLC, St. Petersburg, FL). Hole depth was controlled through careful monitoring of the DRIE etching time. Photoresist was stripped in an Anatech Plasma Asher with an oxygen ashing process (60 minutes, 900 W; Anatech USA, Hayward, CA). To fabricate the step-rigidity substrates, Si wafers were spin-coated with a relatively thick layer of photoresist (S1813; Shipley Company, LLC) and exposed using a contact aligner (ABM-USA, San Jose, CA) to pattern rigidity stripes onto the cylindrical hole array. Photoresist exposure was controlled such that photoresist on the surface of

the Si wafer dissolved during development but photoresist remained within the cylindrical holes to protect them during subsequent etching. Subsequent DRIE etching etched the top surface of the Si wafer without impacting hole depth. Photoresist was stripped in an Anatech Plasma Asher, and substrates were silanized with (1H,1H,2H,2H-Perfluorooctyl)Trichlorosilane as an anti-stiction coating to encourage PDMS release during subsequent replica-molding (MVD100; Applied Microstructures, San Jose, Ca). Replica-molding of silicon masters was performed through pouring of de-gassed PDMS prepolymer (Sylgard 184; Dow Corning, Midland MI), curing for 12 h at 60 °C, and peeling in the presence of 100% ethanol. Ethanol was then removed through critical point drying (EMS 850; Electron Microscopy Sciences, Hartfield, PA). Prior to seeding, substrates were treated with UV for 15 minutes, plasma-treated, uniformly coated with 200 µg/mL human fibronectin for 1 h (BD Biosciences, San Jose, CA), and rinsed with PBS. Spring constants of micropillars were calculated according to the Euler-Bernoulli beam theory equation:  $k = 3EI/L^3$  in which  $k$ ,  $E$ ,  $I$ , and  $L$  are the micropillar spring constant, Young's modulus of PDMS, moment of inertia, and height of the micropillar, respectively.<sup>24</sup> To measure the Young's modulus of PDMS, dimensionally calibrated macroscopic cylinders of PDMS were subjected to normal strain under unconfined compression yielding a Young's modulus of  $0.51 \pm 0.04$  MPa (ElectroForce TA Instruments Mechanical Tester, Model 3100 equipped with 25 N load cell; New Castle, DE).<sup>30</sup>

#### *Cell culture and reagents*

Bovine aortic endothelial cells (BAEC) purchased from VEC technologies (Rensselaer, NY) were used from passages 7-12, and human umbilical vein endothelial cells (HUVEC) purchased from Lonza (Basel, Switzerland) were used from passages 4-5. Endothelial cells were maintained at 37 °C and 5% CO<sub>2</sub>. BAEC were maintained in Medium 199 (Invitrogen, Carlsbad, CA) with 10% Fetal Clone III (HyClone, Logan, UT), 1% MEM amino acids (Invitrogen), 1% MEM vitamins (Mediatech, Manassas VA), and 1% penicillin-streptomycin (Invitrogen). HUVEC were maintained in endothelial growth medium (Lonza) supplemented with the EGM BulletKit (2% v/v FBS, Bovine Brain Extract, Ascorbic Acid, Hydrocortisone, Epidermal Growth Factor, Gentamicin/Amphotericin-B; Lonza).

#### *Immunofluorescence*

Endothelial cells were fixed with 3.7% formaldehyde (Sigma-Aldrich, St. Louis, MO) and permeabilized with 1% Triton (VWR, Radnor PA). VE-cadherin was immunostained with either a goat polyclonal primary antibody (Santa Cruz Biotechnology, Dallas, TX; sc-6459) with an Alexa Fluor 568 donkey anti-goat secondary antibody (Invitrogen; A11055) for neutrophil transmigration percentage studies or a rabbit polyclonal primary antibody (abcam, Cambridge, MA; ab-33168) with an Alexa Fluor 568 donkey anti-rabbit secondary antibody (Invitrogen; A10042) for VE-cadherin junction width and focal adherens junction studies. Vinculin was immunostained with a mouse monoclonal primary antibody (Sigma; V9131) with an Alexa Fluor 488 donkey anti-mouse secondary antibody (Invitrogen; A21202). Nuclei were stained with 4',6-diamidino-2-phenylindole (DAPI) (Sigma). Human neutrophils were immunostained with Alexa Fluor 488-conjugated anti-human CD45 antibody (Biolegend, San Diego, CA; Cat #304017).

#### *Quantification of confluent and sub-confluent cell area*

For measurement of sub-confluent cell area, bovine aortic endothelial cells were seeded as single cells upon fibronectin-coated micropillar substrates and permitted to attach for 18 h. Endothelial cells were then live-labeled with CellTracker Orange (ThermoFisher Scientific, Waltham, MA), fixed, and imaged using a Zeiss LSM700 inverted microscope equipped with a 20X objective. For measurement of confluent cell area, bovine aortic endothelial cells were grown to confluence upon fibronectin-coated micropillar substrates, fixed, and immunostained for VE-cadherin. Cell area, as demarcated by fluorescent images of VE-cadherin-

labeled intercellular boundaries, was quantified using ImageJ software (v. 1.51s; National Institutes of Health, Bethesda, MD).

#### *Quantification of VE-cadherin junction width*

Confluent monolayers of bovine aortic endothelial cells were treated with 10  $\mu$ M Y-27632 for 30 minutes (VWR), bovine thrombin for 5 minutes (4 U/mL; Calbiochem, Darmstadt, Germany), or DMSO vehicle control for 30 minutes (0.1% v/v; Sigma) prior to fixation and immunostaining for VE-cadherin. Images were acquired using a Zeiss LSM700 inverted microscope equipped with a 40X water-immersion objective. VE-cadherin junction width was quantified using ImageJ and a custom-written MATLAB algorithm as described previously.<sup>2</sup> Briefly, images of VE-cadherin were overlaid with a grid containing 16 squares (1600  $\mu$ m<sup>2</sup> per square). The widest junction within each square was measured by drawing a perpendicular line across the junction to obtain the pixel intensity profile. Pixel intensity profiles were fit to a two-Gaussian curve in MATLAB. Junctional width was defined as the width of the two-Gaussian fit 20% above background pixel intensity.

#### *Vinculin focal adhesion quantification and cell-cell junction localization*

Confluent monolayers of bovine aortic endothelial cells were treated with 10  $\mu$ M Y-27632 for 30 minutes (VWR), bovine thrombin for 5 minutes (Calbiochem), or DMSO vehicle control for 30 minutes (0.1% v/v; Sigma) prior to fixation and immunostaining for VE-cadherin, vinculin, and nuclei. Confocal z-stack images were acquired using a Zeiss LSM700 inverted microscope equipped with a 100X oil-immersion objective. Vinculin co-localization with VE-cadherin-stained adherens junctions was quantified with a custom-written MATLAB algorithm as described previously.<sup>31</sup> Briefly, individual images were subjected to an adaptive Wiener filter (1.25  $\mu$ m filtering window) to remove background noise, top-hat filtered (1  $\mu$ m diameter disk), converted to binary with Otsu's method, and median filtered (0.5  $\mu$ m for VE-cadherin and 1  $\mu$ m for vinculin filtering window). Finally, DAPI-labeled nuclei were used to filter out non-specific VE-cadherin signal observed in the nucleus. To quantify VE-cadherin and vinculin co-localization, corresponding filtered images were overlaid to generate 3D overlapping volume data.

Focal adhesion area and quantity was quantified through max intensity projection of z-stack images of VE-cadherin and vinculin, and filtering with a custom-written MATLAB algorithm. VE-cadherin was filtered as described, while vinculin was filtered with an adaptive Wiener filter (0.6  $\mu$ m filtering window), top-hat filtered (1  $\mu$ m diameter disk), converted to binary with Otsu's method, and median filtered (0.6  $\mu$ m filtering window). VE-cadherin-stained adherens junctions were used as a mask to remove vinculin associated with adherens junctions. Speckle noise associated with filtering was reduced through excluding structures smaller than 0.4  $\mu$ m<sup>2</sup>. To quantify vinculin-labeled focal adhesion size and quantity, connected component analysis was performed on corresponding filtered images.

#### *Neutrophil transmigration*

All human subject protocols have been approved by the Institutional Review Board for Human Participants at Cornell University and informed consent was obtained from human subjects. Fresh peripheral human blood was collected into vacutainer tubes containing heparin and permitted to equilibrate at room temperature. Blood was layered over 1-Step Polymorphs (Accurate Chemical, Westbury, NY) and separated by centrifugation. The neutrophil layer was collected, contaminating red blood cells were lysed, and neutrophils were re-suspended in HBSS (VWR). HUVEC monolayers were pretreated with recombinant human TNF- $\alpha$  (0.1 ng/mL; R&D Systems, Minneapolis, MN) for 6 h. Neutrophils (100,000 cells/cm<sup>2</sup>) were then allowed to adhere and extravasate. To quantify the percentage of neutrophils that transmigrated through the endothelium, neutrophils were permitted to extravasate for 30 minutes prior to

gentle washing, fixation, and immunostaining for VE-cadherin for HUVEC and anti-human CD45 for neutrophils as described. Confocal images were acquired using a Zeiss LSM880 upright microscope equipped with a 20X dipping lens objective. The position of neutrophils relative to the endothelium was quantified through manual inspection of XZ orthogonal views created from confocal z-stack images within ImageJ. Transmigrated neutrophils were defined as CD-45-positive cells with greater than 50% of its cell body beneath the endothelial layer. Percentage transmigration was calculated by dividing the number of transmigrated neutrophils by the total number of neutrophils observed within a field of view. To quantify the location and timing of transmigration events, the intercellular junctions of HUVEC were labeled with a non-function blocking, monoclonal antibody conjugated to Dylight-488 against domain 4 of human VE-cadherin (clone hec1) as performed previously.<sup>32,33</sup> Hec1-Dylight-488 was a kind gift from Dr. William A. Muller (Northwestern University, Feinberg School of Medicine, Chicago, IL). Neutrophils were permitted to extravasate for 45 minutes in an environmentally controlled chamber during which time-lapse images were acquired every 20 seconds using a Zeiss LSM700 inverted microscope equipped with a 40X objective. Concurrent imaging of fluorescently labeled intercellular junctions and neutrophil transmigration with transmitted light images permitted identification of the time and location of transmigration events relative to stiff and compliant sub-regions of step-rigidity substrates. To compare the frequency of transmigration within each sub-region, the number of neutrophils that transmigrated within each sub-region was normalized by the area fraction available for transmigration and expressed as a ratio.

#### *Statistical analysis*

All analyses were completed with GraphPad Prism 7 (GraphPad Software Inc, La Jolla, CA). Normality testing was performed with the D'Agostino-Pearson omnibus test. Parametric one-way analysis of variance (ANOVA) followed by Tukey's honestly significant difference (HSD) post hoc testing was performed for VE-cadherin and vinculin co-localization and neutrophil transmigration percentage analyses. Nonparametric Kruskal-Wallis ANOVA followed by Dunn's post-hoc testing was performed for VE-cadherin junction width analyses, sub-confluent and confluent cell area analyses, and focal adhesion comparisons between whole substrates. Comparison of focal adhesion counts within stiff and compliant sub-regions of step-rigidity substrates was performed with a two-tailed Student's t-test, while comparison of focal adhesion area and neutrophil transmigration location and time within stiff and compliant sub-regions of step-rigidity substrates was performed with a two-tailed Mann-Whitney test. *P* values < 0.05 were considered significant.

## **Results**

### *Geometric control of substrate rigidity with micropillars*

To select micropillar substrates with physiologically relevant rigidity, bovine aortic endothelial cells (BAEC) were seeded upon micropillars with a wide range of rigidities. Micropillar diameter (2  $\mu\text{m}$ ) and spacing (4  $\mu\text{m}$  center-to-center) remained consistent and were selected so as to permit endothelial spreading and monolayer formation.<sup>25,30</sup> Substrate rigidity was controlled by varying micropillar height from 12  $\mu\text{m}$  to 3.2  $\mu\text{m}$ , generating micropillars with spring constants from 1 to 54 nN/ $\mu\text{m}$ . Single endothelial cell area was equivalent on relatively compliant micropillars, 1 to 5 nN/ $\mu\text{m}$ , which correspond to effective moduli of 0.7 to 3 kPa on continuous substrates (Figure 1a & 1b).<sup>34</sup> Beyond 5 nN/ $\mu\text{m}$ , single cell area increased with increasing micropillar rigidity indicating endothelial cells are sensing and responding to increasing substrate stiffness as reported by others.<sup>17,35</sup> In contrast, confluent cell area was insensitive to micropillar rigidity, a finding in agreement with previous studies (Figure 1c & 1d).<sup>36</sup>

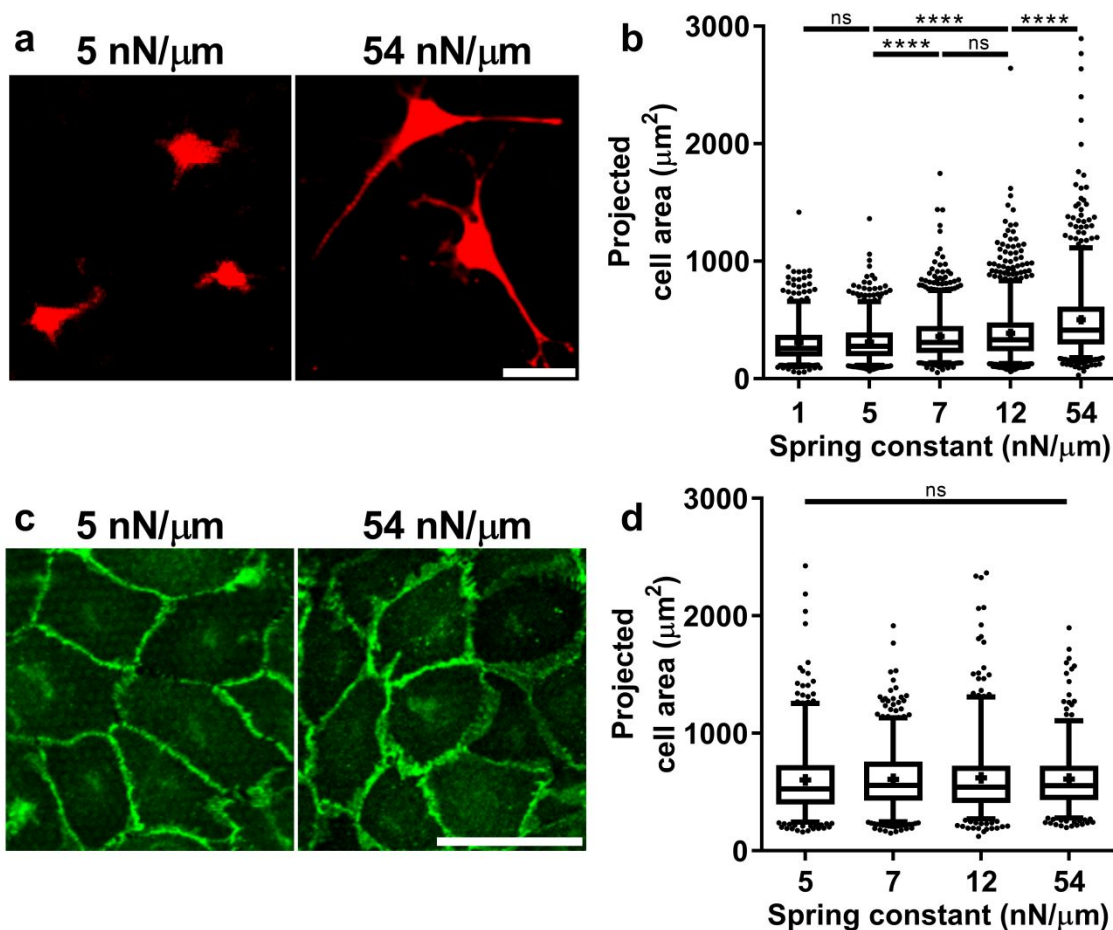


**Figure 1:** Bovine aortic endothelial cells respond to increased uniform substrate rigidity. (a) Single cells on compliant (left) and stiff (right) micropillar arrays (b) Quantification of single cell area as a function of uniform micropillar stiffness ( $n = 542$  cells from 5 chips, 650 cells from 8 chips, 954 cells from 8 chips, 1211 cells from 9 chips, and 811 cells from 7 chips for 1, 5, 7, 12, and 54 nN/ $\mu\text{m}$ , respectively). (c) Confluent cells on compliant (left) and stiff (right) micropillar arrays. (d) Quantification of cell area in confluent monolayers as a function of uniform micropillar stiffness ( $n = 412$  cells from 3 chips, 571 cells from 7 chips, 411 cells from 4 chips, and 375 cells from 3 chips for 5, 7, 12, and 54 nN/ $\mu\text{m}$ , respectively). Data shown as median  $\pm$  interquartile range (box), 5<sup>th</sup>-95<sup>th</sup> percentiles (whiskers), and mean (+). Significance tested using nonparametric Kruskal-Wallis ANOVA followed by Dunn's post-hoc testing; \*\*\*\*  $p < 0.0001$ . Scale bars, 50  $\mu\text{m}$ .

To introduce subcellular scale changes in substrate rigidity, silicon master molds with step-changes in rigidity were fabricated in a two-step deep reactive-ion etching protocol developed previously (Figure 2a).<sup>20</sup> Replica molding of silicon molds yielded co-planar micropillars with step-changes in pillar height (Figure 2b). Rigidity stripes were designed to be closely spaced (20  $\mu\text{m}$  apart) such that each endothelial cell within a monolayer is in contact with both stiff and compliant micropillars (Figure 2c & 2d). Slight expansion of stiff sub-region area was observed with the result that step-rigidity substrates presented cells with 55 % stiff and 45 % compliant area. The rigidity of compliant sub-regions was designed to mimic young, compliant arteries as a spring constant of 5 nN/ $\mu\text{m}$  corresponds to an effective Young's modulus of 3.3 kPa and is

similar to the rigidity of subendothelial matrix in bovine carotid arteries, reported as  $2.7 \pm 1.1$  kPa.<sup>34,37</sup> Stiff sub-regions were fabricated as 2.5-fold stiffer, with  $12 \text{ nN}/\mu\text{m}$  representing an effective Young's modulus of 8 kPa and represents a rigidity range known to alter endothelial barrier integrity.<sup>2</sup>

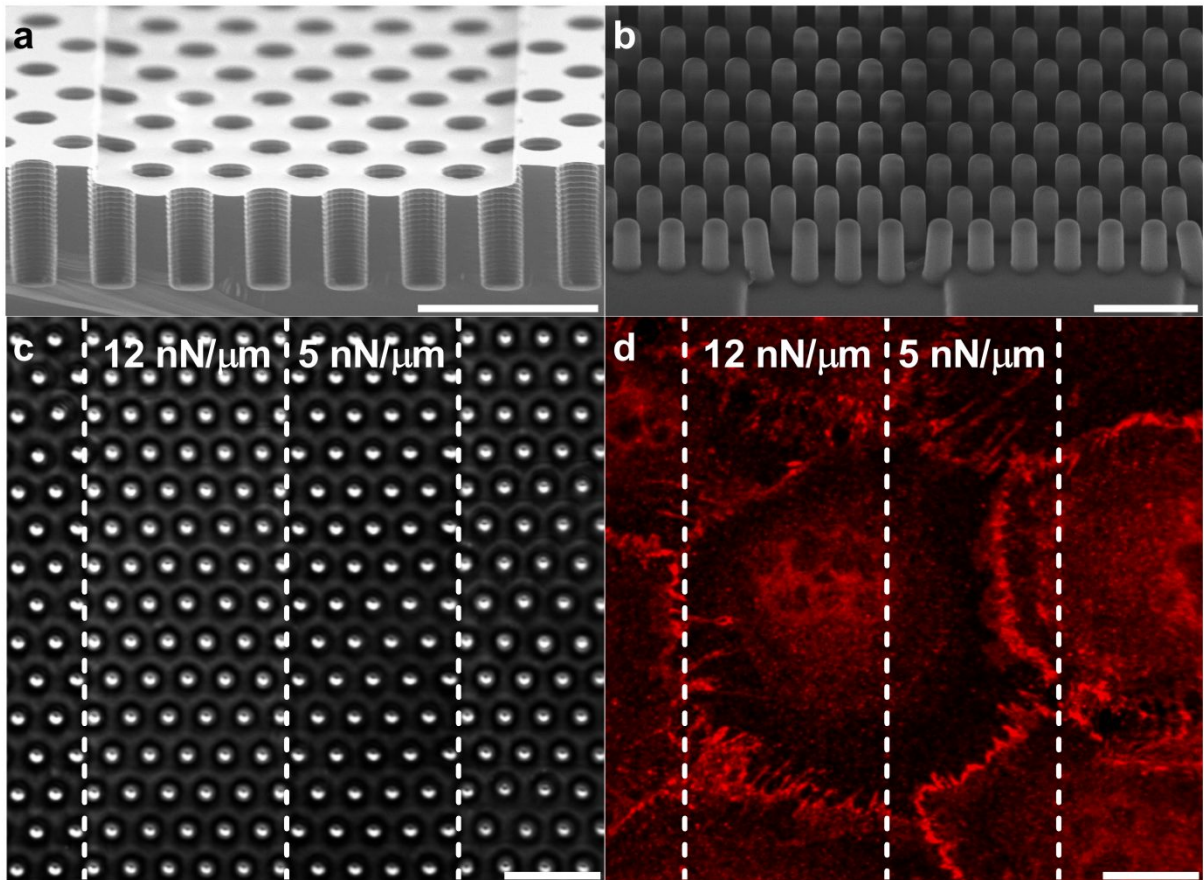


**Figure 2:** Geometric control of substrate rigidity. (a) Scanning electron microscopy (SEM) cross-section image of silicon master mold for step-rigidity substrate. (b) SEM image of PDMS micropillars cast from a step-rigidity master mold. (c) Bright-field of micropillars and (d) corresponding immunofluorescent image of BAEC immunostained for VE-cadherin on a step-rigidity substrate. Scale bars,  $10 \mu\text{m}$ .

#### *Heterogeneous substrate rigidity induces adherens junction disruption through enhanced tension*

Noting that endothelial adherens junctions (AJ) act as regulators of endothelial barrier integrity and noting that increasing substrate rigidity has been found to disrupt AJs previously, we first characterized the morphology of endothelial AJs within monolayers cultured upon step-rigidity substrates relative to stiffness-matched, uniformly stiff controls.<sup>2,22,31</sup> BAEC were grown to confluence, fixed, and immunostained for VE-cadherin, the primary constituent of AJs (Figure 3a). VE-cadherin junction width increased with substrate rigidity which is consistent with previous findings and correlates with reduced endothelial barrier integrity (Figure 3b).<sup>2,31,38</sup> Notably, VE-cadherin junction width was equivalent within monolayers cultured on step-rigidity and rigidity-matched, uniformly stiff substrates. Previous studies have implicated increased Rho-mediated contractility as a mediator of substrate stiffness-mediated disruption in AJs.<sup>2,31</sup> In agreement with previous reports, upregulation of Rho-mediated actomyosin-contraction with thrombin treatment increases junction width, while the opposite is observed with inhibition of Rho-mediated contractility with the ROCK inhibitor Y-27632.<sup>2,39</sup>

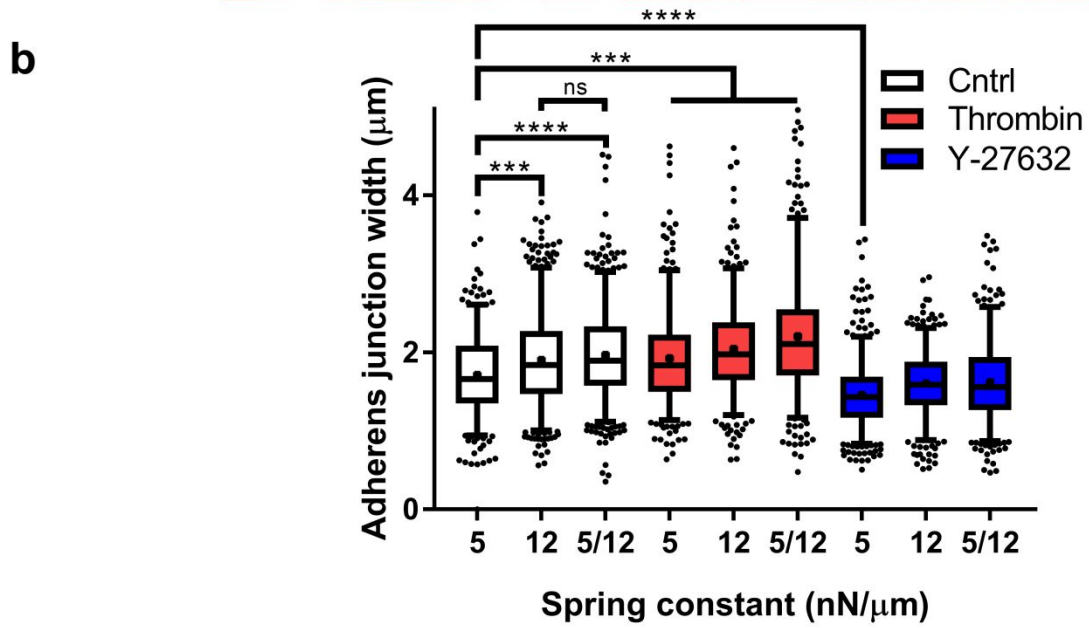
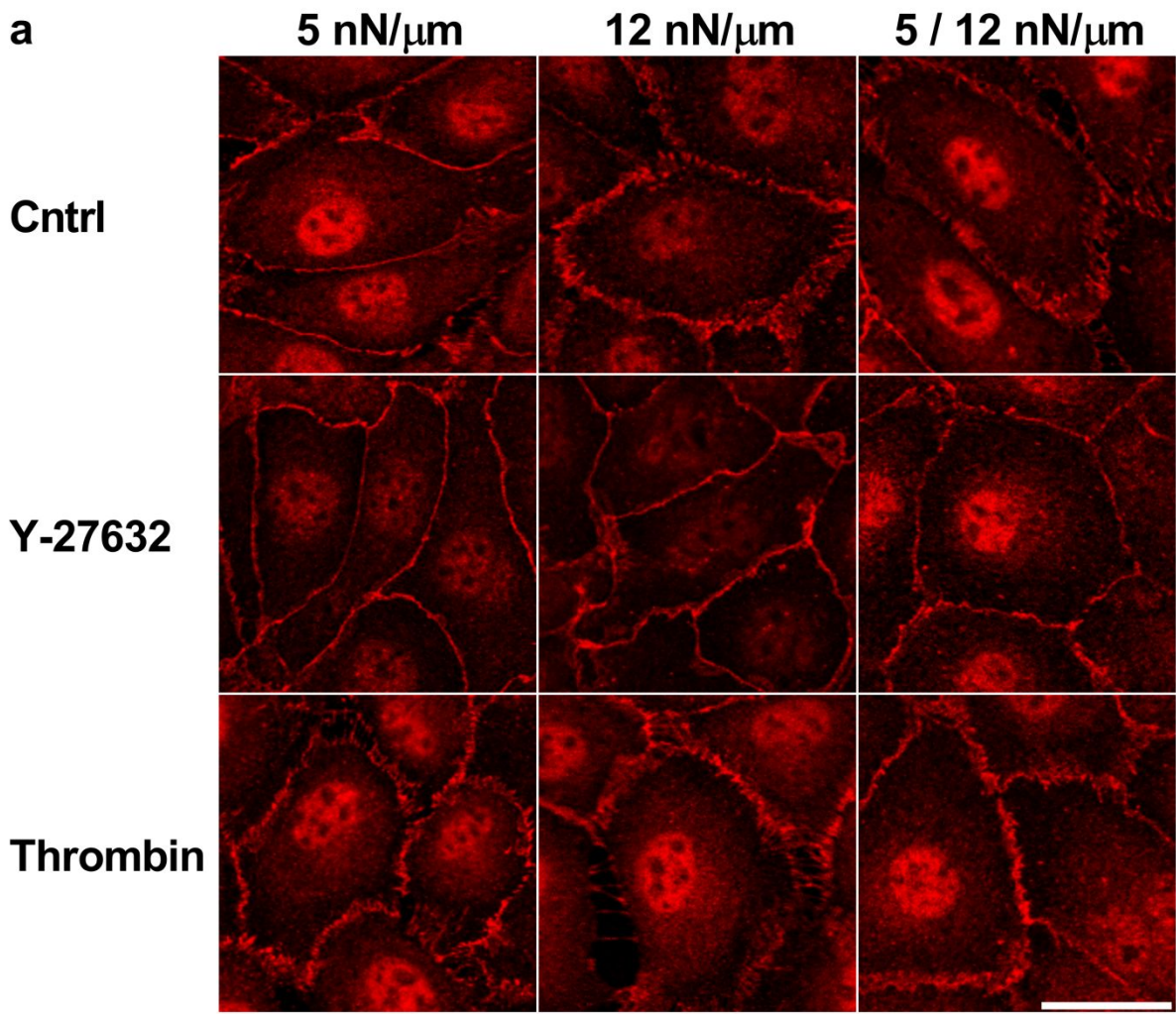


**Figure 3:** Step-rigidity and uniformly stiff substrates disrupt endothelial adherens junctions. (a) Representative images of BAEC adherens junctions from monolayers grown to confluence on uniformly compliant, uniformly stiff, or step-rigidity micropillar substrates, treated with vehicle control, thrombin, or Y-27632, and immunostained for VE-cadherin. (b) Quantification of VE-cadherin junction width of BAEC treated with vehicle control ( $n = 380$  junctions from 4 chips, 569 junctions from 5 chips, and 571 junctions from 6 chips for 5, 12, and 5/12 nN/ $\mu\text{m}$ , respectively), thrombin ( $n = 399$  junctions from 4 chips, 376 junctions from 4 chips, and 393 junctions from 3 chips for 5, 12, and 5/12 nN/ $\mu\text{m}$ , respectively), or Y-27632 ( $n = 506$  junctions from 5 chips, 425 junctions from 4 chips, and 412 junctions from 5 chips for 5, 12, and 5/12 nN/ $\mu\text{m}$ , respectively). Data shown as median  $\pm$  interquartile range (box), 5<sup>th</sup>-95<sup>th</sup> percentiles (whiskers), and mean (+). Significance tested using nonparametric Kruskal-Wallis ANOVA followed by Dunn's post-hoc testing; \*\*\*  $p < 0.001$ , \*\*\*\*  $p < 0.0001$ . Scale bar, 25  $\mu\text{m}$ .

To investigate the mechanism by which junctions are being altered by matrix rigidity, we characterized intercellular tension based on the localization of the mechano-sensitive protein vinculin at the junctions.<sup>31</sup> Vinculin is recruited to intercellular junctions under elevated tension, an effect that can be stimulated with endothelial hormones such as thrombin.<sup>40,41</sup> Furthermore, vinculin recruitment to AJs is enhanced by increased matrix stiffness and correlates with increased VE-cadherin junction width and enhanced endothelial permeability.<sup>31</sup> Vinculin recruitment in our system was measured through co-localization analysis of immunostained VE-cadherin with vinculin within confluent monolayers (Figure 4a). VE-cadherin:vinculin co-localization volume significantly increased with increasing micropillar rigidity, while monolayers cultured on step-rigidity substrates exhibited similar co-localization to those on rigidity-matched stiff substrates (Figure 4b). Surprisingly, thrombin treatment did not enhance VE-cadherin:vinculin co-localization on stiff or step-rigidity substrates relative to their respective vehicle controls, but rather appeared to plateau. In contrast, ROCK inhibition with Y-27632 treatment significantly reduced VE-cadherin:vinculin co-localization within monolayers on all substrates to levels equivalent with control-treated compliant substrates. Together, these data suggest that heterogeneous matrix rigidity disrupts intercellular AJs equivalently to rigidity-matched stiff substrates through enhanced intercellular tension.

We next sought to ask whether our observed increase in vinculin recruitment to AJs is limited to stiff sub-regions of step-rigidity substrates, or if junction remodeling occurs throughout monolayer regions within both stiff and compliant sub-regions. To address this, we compared VE-cadherin:vinculin co-localization volumes within stiff and compliant sub-regions. Co-localization volumes were normalized by the area fraction of each sub-region to account for stiff sub-regions being slightly larger than compliant sub-regions. Surprisingly, the ratio of VE-cadherin:vinculin co-localization volume within monolayer regions positioned on stiff and compliant sub-regions is equal (Figure 4c). Thus, these data suggest that heterogeneous matrix rigidity presented by step-rigidity substrates leads to remodeling of intercellular junctions throughout the entire monolayer.

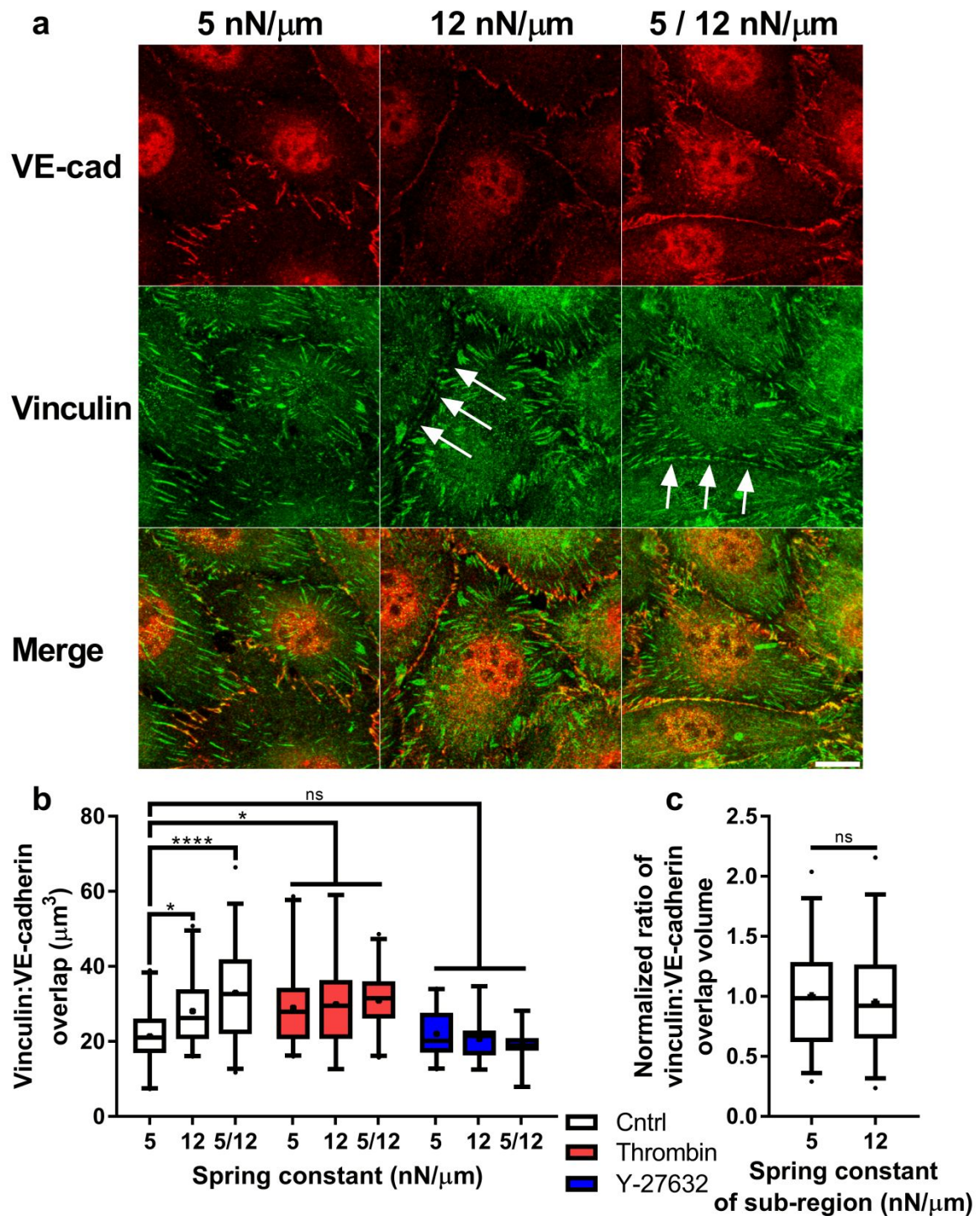


**Figure 4:** Endothelial monolayers on step-rigidity and uniformly stiff substrates exhibit increased intercellular tension relative to uniformly compliant substrates. (a) Representative images of BAEC monolayers grown to confluence on uniformly compliant, uniformly stiff, or step-rigidity micropillar substrates, treated with vehicle control, and immunostained for VE-cadherin and vinculin. Arrows depict vinculin recruitment to adherens junctions. (b) Quantification of volume of VE-cadherin:vinculin colocalization of BAEC treated with vehicle control ( $n = 27$  regions from 5 chips, 31 regions from 6 chips,

and 32 regions from 6 chips for 5, 12, and 5/12 nN/ $\mu\text{m}$ , respectively), thrombin ( $n = 21$  regions from 4 chips, 18 regions from 3 chips, and 25 regions from 5 chips for 5, 12, and 5/12 nN/ $\mu\text{m}$ , respectively), or Y-27632 ( $n = 22$  regions from 4 chips, 18 regions from 3 chips, and 18 regions from 3 chips for 5, 12, and 5/12 nN/ $\mu\text{m}$ , respectively). (c) Quantification of ratio of VE-cadherin:vinculin co-localization overlap volume within stiff and compliant sub-regions of step-rigidity substrates ( $n = 32$  stiff and compliant sub-regions from 5 chips). Data shown as median  $\pm$  interquartile range (box), 5<sup>th</sup>-95<sup>th</sup> percentiles (whiskers), and mean (+). Significance tested using 1-way ANOVA followed by tukey post-hoc testing (b) and two-tailed Mann-Whitney test (c); \*  $p < 0.05$ , \*\*\*\*  $p < 0.0001$ . Scale bar, 10  $\mu\text{m}$ .

### *Stiff rigidities dictate leukocyte transmigration percentage on substrates of heterogeneous rigidity*

To further investigate the impact of heterogeneous matrix rigidity upon endothelial barrier integrity, we asked whether heterogeneous matrix rigidity promoted an increase in the percentage of leukocyte transmigration through the endothelium. Primary human neutrophils were isolated and seeded onto confluent human umbilical vein endothelial cells (HUVEC) stimulated with TNF-alpha. Following a fixed time period of extravasation, HUVEC and neutrophils were fixed and immunostained for VE-cadherin and CD-45, respectively, with extravasation events defined as neutrophils having greater than 50% of their cell body beneath the endothelial monolayer (Figure 5a). Similar to prior studies, we found that increasing micropillar rigidity increased the percentage of neutrophils that transmigrated through the endothelium (Figure 5b).<sup>2,11</sup> To test the impact of stiff sub-regions on the frequency of leukocyte transmigration frequency, we fabricated and tested step-rigidity substrates with different pairings of compliant and rigid sub-regions. Notably, regardless of the pairing between compliant and rigid sub-regions, we found that the percentage of neutrophil transmigration was primarily dictated by the rigidity of the stiff sub-region (Figure 5b). Previous reports have established that leukocyte capture under blood-mimicking flow, and expression of intercellular adhesion molecule 1 (ICAM-1), vascular cell adhesion molecule 1 (VCAM-1) and E-selectin do not change as a function of matrix stiffness.<sup>2,9,11</sup> Thus, as opposed to differential up-regulation of inflammatory molecules, these results suggest increased leukocyte transmigration observed on uniformly stiff and step-rigidity substrates is due to disrupted adherens junctions and barrier integrity.

Given the dominating effects of stiff sub-regions, we next sought to pinpoint the locations of neutrophil transmigration events to determine whether neutrophils preferentially extravasate within stiff sub-regions of step-rigidity micropillar arrays. Selecting one step-rigidity substrate pairing, we performed time-lapse imaging of neutrophil extravasation through TNF-alpha-stimulated HUVEC monolayers labeled with a non-function blocking antibody against VE-cadherin (for representative time-lapse, see Movie S1).<sup>32</sup> As expected and consistent with a previous report that utilized micropillars, neutrophils induced VE-cadherin gap formation at cell-cell junctions during transmigration and after transmigration neutrophils randomly migrated underneath the endothelium (Figure 5c and Movie S1).<sup>30</sup> Throughout each time-lapse movie, the location of each neutrophil transmigration event was recorded and noted as occurring within either the stiff or the compliant sub-region. To compare the frequency of transmigration within each sub-region, the number of neutrophils that transmigrated within each sub-region was normalized by the area fraction available for transmigration to account for stiff sub-regions being slightly larger than compliant sub-regions. Surprisingly, the ratio of neutrophil transmigration through endothelium positioned on stiff and compliant sub-regions is equal (Figure 5d). To further characterize potential differences in barrier disruption between stiff and compliant sub-regions, the time for neutrophil transmigration events within each sub-region was measured and found to be statistically equivalent (Figure 5e). Together, these data indicate that stiff sub-regions of step-rigidity substrates dictate the degree of endothelial barrier integrity disruption, and barrier disruption is not confined to regions of the endothelium positioned on stiff sub-regions.

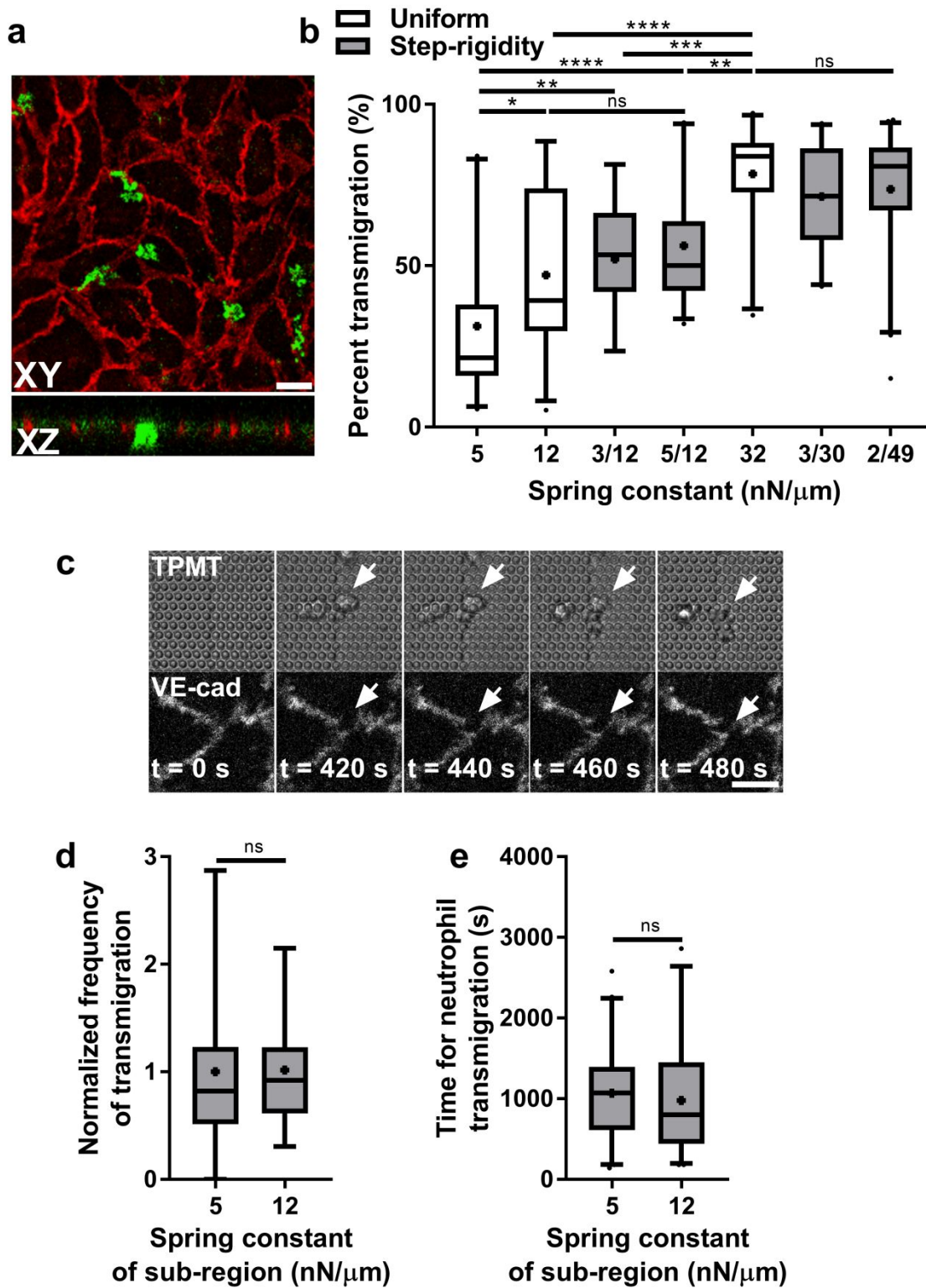


**Figure 5:** Human umbilical vein endothelial cell (HUVEC) monolayers on step-rigidity substrates recruit leukocytes with equivalent percentage to monolayers on rigidity-matched, uniformly stiff substrates. (a)

Representative max-intensity projection and XZ orthogonal view of a HUVEC monolayer fixed following 30 minutes of neutrophil transmigration. Intercellular junctions and neutrophils were immunostained with antibodies against VE-cadherin (red) and CD-45 (green), respectively. (b) Quantification of transmigration percentage ( $n = 29$  regions from 5 chips, 24 regions from 4 chips, 22 regions from 4 chips, 18 regions from 3 chips, 30 regions from 5 chips, 24 regions from 4 chips, and 44 regions from 7 chips for 5, 12, 32, 3/12, 5/12, 3/30, and 2/49 nN/ $\mu\text{m}$ , respectively). (c) Representative time-lapse sequence depicting neutrophil transmigration. Neutrophils were observed with transmitted light (TPMT), while a conjugated, non-function blocking antibody against VE-cadherin (VE-cad) permitted visualization of gap formation during neutrophil transmigration (arrow). (d) Quantification of ratio of neutrophil transmigration on stiff and compliant sub-regions of step-rigidity substrates ( $n = 92$  neutrophils observed over 16 chips). (e) Quantification of time for neutrophil transmigration events on stiff and compliant sub-regions of step-rigidity substrates ( $n = 92$  neutrophils observed over 16 chips). Data shown as median  $\pm$  interquartile range (box), 5<sup>th</sup>-95<sup>th</sup> percentiles (whiskers), and mean (+). Significance tested using 1-way ANOVA followed by tukey post-hoc testing (b) and two-tailed Mann-Whitney test (d, e); \*  $p < 0.05$ , \*\*  $p < 0.01$ , \*\*\*  $p < 0.001$ , \*\*\*\*  $p < 0.0001$ . Scale bars, 20  $\mu\text{m}$ .

*Focal adhesions in the entire cell remodel in response to the stiffest matrix encountered*

Given our results indicate that stiff sub-regions of step-rigidity substrates are impacting adherens junction morphology and leukocyte transmigration, and noting that rigidity sensing is mediated by focal adhesions, we next asked how heterogeneous matrix rigidity impacted focal adhesion morphology.<sup>16,17</sup> Endothelial monolayers grown to confluence on micropillar arrays were immunostained for vinculin to identify focal adhesions and VE-cadherin to filter signal associated with vinculin recruitment to adherens junctions. Consistent with a recent report, increased matrix stiffness correlated with significantly increased focal adhesion count per cell but surprisingly, focal adhesion area was unchanged (Figure 6a & 6b).<sup>42</sup> Notably, focal adhesion count per cell within endothelial monolayers cultured upon step-rigidity substrates was identical to rigidity-matched stiff substrates.

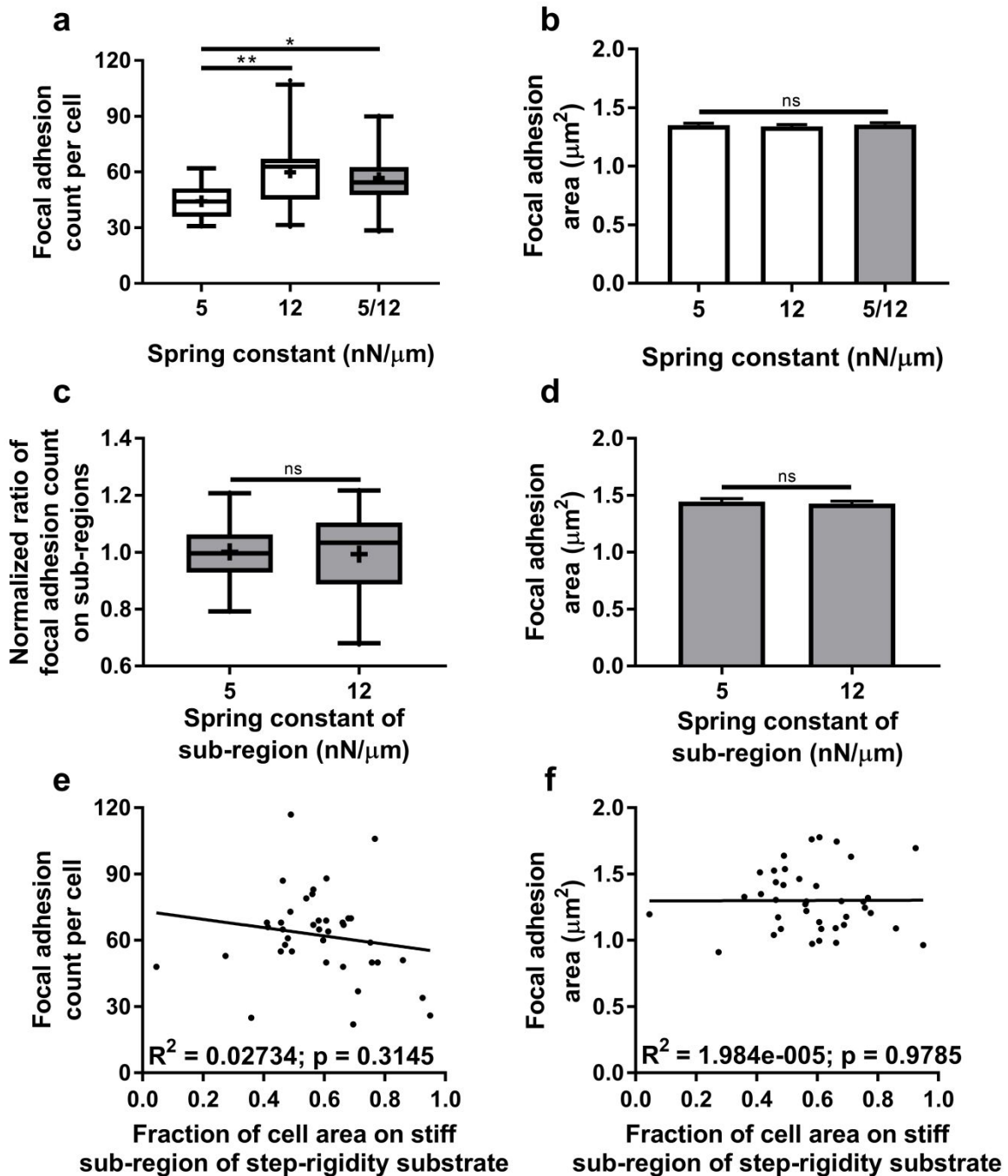


**Figure 6:** Focal adhesion density, but not size increases within monolayers cultured on step-rigidity substrates and uniformly stiff substrates relative to uniformly compliant substrates. (a) Quantification of focal adhesion count per cell ( $n = 21$  regions from 4 chips for 5, 12, and 5/12 nN/ $\mu\text{m}$ ) and (b) focal adhesion area ( $n = 6547, 6747,$  and  $6437$  focal adhesions from 4 chips for 5, 12, and 5/12 nN/ $\mu\text{m}$ , respectively) within monolayers cultured on uniformly compliant, uniformly stiff, or step-rigidity substrates. (c) Quantification of ratio of focal adhesion count ( $n = 20$  regions from 4 chips for 5 and 12 nN/ $\mu\text{m}$ ) and (d) focal adhesion area ( $n = 3451$  and  $4126$  focal adhesions from 4 chips for 5 and 12 nN/ $\mu\text{m}$ ,

respectively) within monolayer regions positioned on stiff and compliant sub-regions of step-rigidity substrates. (e) Focal adhesion count per cell and (f) focal adhesion area plotted as a function of cell area positioned on stiff sub-region of step-rigidity substrate ( $n = 39$  cells from 7 chips for focal adhesion count and area). Data are mean  $\pm$  SEM (b, d) and median  $\pm$  interquartile range (box), 5<sup>th</sup>-95<sup>th</sup> percentiles (whiskers), and mean (+) (a, c). Significance tested using nonparametric Kruskal-Wallis ANOVA followed by Dunn's post-hoc testing (a, b), two-tailed Student's t-test (c), two-tailed Mann-Whitney test (d); \*  $p < 0.05$ , \*\*  $p < 0.01$ .

Focal adhesions act as discrete mechanosensors that are capable of responding to the local rigidity of the matrix they encounter.<sup>15</sup> Furthermore, we previously demonstrated that single endothelial cells positioned on an interface of stiff and compliant matrix exhibit increased focal adhesion size within the cell body positioned over stiff matrix.<sup>19</sup> Therefore, we asked whether focal adhesion density or size differs between stiff and compliant sub-regions of step-rigidity substrates. To compare focal adhesion count within each sub-region, focal adhesion locations were determined by the position of the focal adhesion's centroid and the number of focal adhesions in each sub-region was normalized by the area fraction of each sub-region within the field of view. Surprisingly, we did not observe any significant difference in the ratio of focal adhesion count or focal adhesion size between stiff and compliant sub-regions of step-rigidity substrates (Figure 6c & 6d). To further address this question, we asked whether the fraction of endothelial cell area on stiff sub-regions of step-rigidity substrates correlated with increased focal adhesion density or area. Consistent with earlier sub-region data, we did not observe any significant correlation between focal adhesion area or count per cell with respect to the fraction of cell area on stiff sub-regions of step-rigidity arrays (Figure 6e & 6f). Together, our data indicate that stiff sub-regions of heterogeneous micropillar arrays cause endothelial cells within monolayers to remodel their cell-matrix adhesions throughout the entire cell body.

## Discussion

Intimal stiffening drives the progression of atherosclerosis through upregulation of actomyosin contractility and disruption of endothelial adherens junctions, but the impact of complex mechanical cues upon endothelial monolayer behavior is not well studied.<sup>2</sup> Here, we use a micropillar model to introduce closely spaced, subcellular scale stiffness heterogeneities, and our data demonstrate that endothelial monolayers respond by adopting the phenotype associated with the stiffest matrix encountered. As such, endothelial monolayers cultured upon step-rigidity substrates displayed disruption of barrier integrity identical to rigidity-matched, uniformly stiff substrates as evidenced by equivalent disruption of adherens junctions and percentage of leukocyte transmigration. However, we did not observe differences in vinculin recruitment to adherens junctions, leukocyte transmigration frequency or timing, and focal adhesion size or density between sub-regions of step-rigidity substrates.

Endothelial cells sense and respond to matrix stiffness through mechanosensitive, integrin-based focal adhesions that are essential for endothelial adhesion and barrier integrity.<sup>16,17,43-45</sup> Previous studies have demonstrated that focal adhesions within single cells respond to increasing matrix rigidity on continuous, elastic substrates through increasing focal adhesion size, an effect that can be reproduced by application of exogenous force directly to a focal adhesion.<sup>18,31,46,47</sup> Similarly, on discontinuous micropillar substrates, focal adhesion size within single cells has been shown to correlate to local traction stress.<sup>24</sup> However, the relationship between focal adhesion morphology and substrate rigidity within a confluent endothelium is less well studied and more complex than single cells because within an endothelium adjacent cells form an interconnected actomyosin-network through adherens junctions.<sup>23,48,49</sup> A recent report by Andresen Eguiluz *et al.* found that increasing polyacrylamide gel stiffness correlated with increases in both focal adhesion count per cell and focal adhesion size.<sup>42</sup> Here, we tested the influence of substrate rigidity on focal adhesion

morphology within a confluent endothelium and observed increased focal adhesion density, but not size in response to increasing substrate rigidity. The observed disparity between changes in focal adhesion size with respect to substrate rigidity in our systems could be related to the discrete nature of micropillar substrates which may limit focal adhesion reinforcement in response to rigidity.<sup>34</sup> Our results suggest that individual focal adhesions within a monolayer do not experience greater local stress in response to increasing substrate rigidity, but the observed increase in focal adhesion density could represent an increase in basal endothelial tension.<sup>50,51</sup> Consistent with this result, greater vinculin recruitment to adherens junctions observed on uniformly stiff and step-rigidity substrates indicates greater intercellular tension.

<sup>31,40,41</sup>

Leukocyte transmigration is a hallmark of the endothelial inflammatory response and atherosclerotic progression.<sup>52–54</sup> Consistent with previous studies, we found that leukocyte transmigration increases in frequency with increasing matrix stiffness while the frequency of transmigration on step-rigidity substrates was dictated by the stiffest matrix presented to the endothelium.<sup>2,11</sup> However, reverse transendothelial (rTEM) of leukocytes has long been recognized to occur in resolution of the immune response, including atherosclerotic plaque regression, but the mechanism of rTEM is still under investigation.<sup>55–58</sup> Here, neutrophil transmigration percentage was measured with an immunofluorescence-based end-point assay which could not detect rTEM events. However, consistent with a previous report, we did observe rTEM events during time-lapse recordings of neutrophils seeded on TNF-alpha-stimulated endothelial monolayers.<sup>56</sup> Currently, the impact of substrate stiffness on the mechanism or frequency of rTEM is unclear but represents a topic deserving of future study given the potential role intimal stiffening may play in preventing leukocyte rTEM and atherosclerotic plaque regression.

Interestingly, vinculin recruitment to adherens junctions, leukocyte transmigration time and frequency, focal adhesion size, and focal adhesion density was equivalent within monolayer regions positioned on stiff and compliant sub-regions of step-rigidity substrates. This behavior within a confluent endothelium contrasts with a recent report in which single endothelial cells were seeded on an interface of stiff and compliant matrix and focal adhesion size was markedly increased within the cell body positioned on stiff matrix.<sup>19</sup> This discrepancy likely reflects the vastly different mechanical environment experienced by single and confluent endothelial cells. Namely, the interconnected network of actin cytoskeleton-linked adherens junctions permits force transmission to neighboring cells through VE-cadherin complexes, which have previously been identified as force transducers.<sup>21,42</sup> Furthermore, step-rigidity substrates were designed such that each endothelial cell within a monolayer could integrate cues from stiff and compliant sub-regions. Thus, mechanical tension applied by neighboring cells could normalize metrics of mechanotransduction that may show sub-cellular localization in response to heterogeneous matrix rigidity within single cells.

Despite the advantage of the micropillar system in providing geometric control of substrate rigidity, the discrete nature of micropillars does not permit cellular interaction through transmission of forces within the substrate.<sup>59–61</sup> In spite of this limitation, our system overcomes limitations identified in continuous surfaces, like fluctuations in surface topography due to swelling as a function of stiffness.<sup>19,27–29</sup> The micropillar system also enables the testing of a large range of disparities in matrix stiffness, including the 2.5-fold to nearly 25-fold disparities in matrix stiffness between stiff and compliant sub-regions described here. As comparison, nearly 50-fold intimal stiffness heterogeneities have been reported from *ex vivo* mechanical characterization of aged murine intimal tissue in which intimal stiffness could vary from 2 to 100 kPa within a 100 x 100  $\mu\text{m}$  area.<sup>14</sup> Our micropillar substrates were coated uniformly with fibronectin as opposed to microcontact printing. As such, we cannot exclude the possibility of cell adhesion to the sides of pillars which would influence the effective substrate stiffness experienced by endothelial cells. However, the high

density of micropillar arrays restricted cell spreading to the tops of pillars as reported previously with micropillars uniformly coated with fibronectin<sup>25</sup>. Furthermore, we tested a wide range of micropillar heights and validated that endothelial cells responded to the stiffness range presented.

Endothelial monolayers must maintain a delicate balance between cell-matrix and cell-cell adhesion to maintain vascular integrity.<sup>62</sup> It is well established that increasing matrix rigidity upregulates Rho-mediated endothelial cell contractility, disrupting that balance thereby widening adherens junctions, enhancing vascular permeability, and promoting leukocyte transmigration.<sup>2,9-11,13</sup> Our results suggest that closely-spaced heterogeneities in substrate stiffness impact the endothelium similarly, as we observe similar widening and increasing tension at adherens junctions and increased leukocyte transmigration on step-rigidity substrates. Mechanical characterization of aging subendothelial matrix, as well as atherosclerotic plaques have identified significant mechanical heterogeneity that endothelial cells encounter.<sup>14,63,64</sup> Thus, our approach indicates endothelial cells in simultaneous contact with stiff and compliant matrix, as they may experience *in vivo* during pathological arterial remodeling, may respond by adopting a “stiff” phenotype characterized by disrupted barrier integrity. However, our platform did not test how local elevations in substrate stiffness may impact nearby endothelial cells that are only in contact with compliant matrix. Our results indicate that stiff sub-regions are sufficient to increase intercellular tension, but it is currently unclear how this tension may impact neighboring cell contractility or barrier function. Exogenous application of force to VE-cadherin causes disruption of distant intercellular junctions, with disruption observed up to three cell diameters away from the initial perturbation.<sup>21</sup> However, it is currently not clear whether a localized region of increased rigidity would have an analogous, distant impact on nearby cells. Future studies should modulate the presentation and disparity of matrix stiffness heterogeneities to investigate force transmission within endothelial monolayers and resulting impacts on barrier maintenance.

## Conclusions

Microfabricated substrates presenting closely spaced, subcellular scale stiffness heterogeneities were fabricated to investigate the impact of substrate stiffness heterogeneity on endothelial cell behavior. Endothelial monolayers on step-rigidity substrates adopted the phenotype associated with the stiffest matrix they encountered, as evidenced by disruption in adherens junction morphology, increased leukocyte transmigration, and increased focal adhesion density. Our approach enabled us to extend the understanding of how an endothelium might respond to heterogeneities in intimal stiffness reported to develop with age or disease and indicates matrix stiffness heterogeneities could disrupt barrier integrity and contribute to atherogenesis.

## Conflict of Interest Statement

There are no conflicts to declare.

## Acknowledgments

We gratefully acknowledge help and support from Thomas Pennell for nanofabrication support, Dr. Michael King for providing whole blood samples for leukocyte transmigration experiments, Matthew Zanotelli and Dr. Francois Bordeleau for providing a MATLAB script for co-localization analysis, and Dr. William A. Muller for providing a non-function blocking VE-cadherin antibody for live-cell imaging. This work was performed in part at the Cornell NanoScale Facility, a member of the National Nanotechnology Coordinated Infrastructure (NNCI), which is supported by the National Science Foundation (Grant ECCS-1542081). This work made use of the Cornell Center for Materials Research Shared Facilities which are supported through the NSF MRSEC program (DMR-1719875) and Cornell University Institute of Biotechnology which are supported by NIH S10OD018516. This work was supported from grants from the

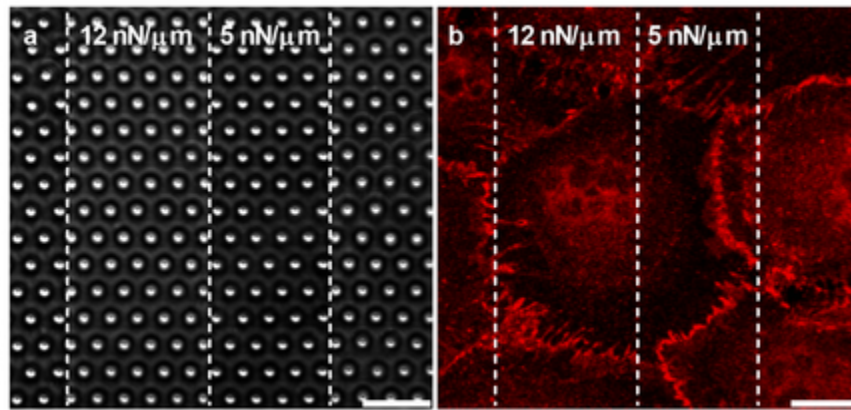
National Science Foundation (award number 1435755) and the National Institutes of Health to C.A.R. (Project number: HL127499), and a Graduate Research Fellowship to J.A.V. under Cornell University NSF Grant DGE-1650441.

## References

- 1 M. J. Paszek, N. Zahir, K. R. Johnson, J. N. Lakins, G. I. Rozenberg, A. Gefen, C. A. Reinhart-King, S. S. Margulies, M. Dembo, D. Boettiger, D. A. Hammer and V. M. Weaver, *Cancer Cell*, 2005, **8**, 241–254.
- 2 J. Huynh, N. Nishimura, K. Rana, J. M. Peloquin, J. P. Califano, C. R. Montague, M. R. King, C. B. Schaffer and C. A. Reinhart-King, *Sci. Transl. Med.*, 2011, **3**, 112ra122–112ra122.
- 3 J. C. Kohn, M. C. Lampi and C. A. Reinhart-King, *Front. Genet.*, 2015, **6**, 112.
- 4 J. Blacher, R. Asmar, S. Djane, G. M. London and M. E. Safar, *Hypertension*, 1999, **33**, 1111–1117.
- 5 T. W. Hansen, J. A. Staessen, C. Torp-Pedersen, S. Rasmussen, L. Thijs, H. Ibsen and J. Jeppesen, *Circulation*, 2006, **113**, 664–670.
- 6 F. U. S. Mattace-Raso, T. J. M. Van Der Cammen, A. Hofman, N. M. Van Popele, M. L. Bos, M. A. D. H. Schalekamp, R. Asmar, R. S. Reneman, A. P. G. Hoeks, M. M. B. Breteler and J. C. M. Witteman, *Circulation*, 2006, **113**, 657–663.
- 7 K. Sutton-Tyrrell, S. S. Najjar, R. M. Boudreau, L. Venkitachalam, V. Kupelian, E. M. Simonsick, R. Havlik, E. G. Lakatta, H. Spurgeon, S. Kritchevsky, M. Pahor, D. Bauer and A. Newman, *Circulation*, 2005, **111**, 3384–3390.
- 8 J. A. Vanderburgh and C. A. Reinhart-King, *The Role of Age-Related Intimal Remodeling and Stiffening in Atherosclerosis*, Elsevier Inc., 1st edn., 2017.
- 9 H. N. Hayenga and H. Aranda-Espinoza, *Cell. Mol. Bioeng.*, 2013, **6**, 253–265.
- 10 R. Krishnan, D. D. Klumpers, C. Y. Park, K. Rajendran, X. Trepap, J. van Bezu, V. W. M. van Hinsbergh, C. V. Carman, J. D. Brain, J. J. Fredberg, J. P. Butler and G. P. van Nieuw Amerongen, *AM J Physiol Cell Physiol*, 2011, **300**, C146–C154.
- 11 K. M. Stroka and H. Aranda-Espinoza, *Blood*, 2011, **118**, 1632–1640.
- 12 R. M. Weisbrod, T. Shiang, L. Al Sayah, J. L. Fry, S. Bajpai, C. A. Reinhart-King, H. E. Lob, L. Santhanam, G. Mitchell, R. a. Cohen and F. Seta, *Hypertension*, 2013, **62**, 1105–1110.
- 13 R. L. Urbano, C. Furia, S. Basehore and A. M. Clyne, *Biophys. J.*, 2017, **113**, 645–655.
- 14 J. C. Kohn, A. Chen, S. Cheng, D. R. Kowal, M. R. King and C. A. Reinhart-King, *J. Biomech.*, 2016, **49**, 1447–53.
- 15 S. V. Plotnikov, A. M. Pasapera, B. Sabass and C. M. Waterman, *Cell*, 2012, **151**, 1513–1527.
- 16 B. Z. Katz, E. Zamir, A. Bershadsky, Z. Kam, K. M. Yamada and B. Geiger, *Mol. Biol. Cell*, 2000, **11**, 1047–1060.
- 17 R. J. J. Pelham and Y.-L. Wang, *Proc. Natl. Acad. Sci.*, 1997, **94**, 13661–13665.
- 18 I. B. Bischofs and U. S. Schwarz, *Proc. Natl. Acad. Sci.*, 2003, **100**, 9274–9279.
- 19 M. C. Lampi, M. Guvendiren, J. A. Burdick and C. A. Reinhart-King, *ACS Biomater. Sci. Eng.*, 2017, **3**, 3007–3016.
- 20 M. T. Breckenridge, R. A. Desai, M. T. Yang, J. Fu and C. S. Chen, *Cell. Mol. Bioeng.*, 2013, **7**, 26–34.
- 21 A. K. Barry, N. Wang and D. E. Leckband, *J. Cell Sci.*, 2015, **128**, 1341–51.
- 22 M. Giannotta, M. Trani and E. Dejana, *Dev. Cell*, 2013, **26**, 441–454.
- 23 M. G. Lampugnani, M. Corada, L. Caveda, F. Breviario, O. Ayalon, B. Geiger and E. Dejana, *J. Cell Biol.*, 1995, **129**, 203–17.
- 24 J. L. Tan, J. Tien, D. M. Pirone, D. S. Gray, K. Bhadriraju and C. S. Chen, *Proc. Natl. Acad. Sci. U. S. A.*, 2003, **100**, 1484–9.
- 25 O. du Roure, A. Saez, A. Buguin, R. H. Austin, P. Chavrier, P. Silberzan and B. Ladoux, *Proc. Natl. Acad. Sci. U. S. A.*, 2005, **102**, 2390–2395.

- 26 M. T. Yang, J. Fu, Y.-K. Wang, R. a Desai and C. S. Chen, *Nat. Protoc.*, 2011, **6**, 187–213.
- 27 J. A. Burdick, C. Chung, X. Jia, M. A. Randolph and R. Langer, *Biomacromolecules*, 2005, **6**, 386–391.
- 28 M. Guvendiren and J. A. Burdick, *Nat. Commun.*, 2012, **3**, 792.
- 29 R. A. Marklein and J. A. Burdick, *Soft Matter*, 2010, **6**, 136–143.
- 30 A. Rabodzey, P. Alcaide, F. W. Lusinskas and B. Ladoux, *Biophys. J.*, 2008, **95**, 1428–1438.
- 31 M. C. Lampi, C. J. Faber, J. Huynh, F. Bordeleau, M. R. Zanotelli and C. A. Reinhart-King, *PLoS One*, 2016, **11**, 1–20.
- 32 A. M. Gonzalez, B. F. Cyrus and W. A. Muller, *Am. J. Pathol.*, 2016, **186**, 1387–1402.
- 33 J. Ali, F. Liao, E. Martens and W. A. Muller, *Microcirculation*, 1997, **4**, 267–277.
- 34 M. Ghibaud, A. Saez, L. Trichet, A. Xayaphoummine, J. Browaeys, P. Silberzan, A. Buguin and B. Ladoux, *Soft Matter*, 2008, **4**, 1836.
- 35 J. P. Califano and C. A. Reinhart-King, *J. Biomech.*, 2010, **43**, 79–86.
- 36 T. Yeung, P. C. Georges, L. A. Flanagan, B. Marg, M. Ortiz, M. Funaki, N. Zahir, W. Ming, V. Weaver and P. A. Janmey, *Cell Motil. Cytoskeleton*, 2005, **60**, 24–34.
- 37 J. Peloquin, J. Huynh, R. M. Williams and C. A. Reinhart-King, *J. Biomech.*, 2011, **44**, 815–821.
- 38 F. Bordeleau, B. N. Mason, E. M. Lollis, M. Mazzola, M. R. Zanotelli, S. Somasegar, J. P. Califano, C. Montague, D. J. LaValley, J. Huynh, N. Mencia-Trinchant, Y. L. Negrón Abril, D. C. Hassane, L. J. Bonassar, J. T. Butcher, R. S. Weiss and C. A. Reinhart-King, *Proc. Natl. Acad. Sci.*, 2017, **114**, 492–497.
- 39 N. V Bogatcheva, J. G. Garcia and A. D. Verin, *Biochem.*, 2002, **67**, 75–84.
- 40 S. Huvneers, J. Oldenburg, E. Spanjaard, G. van der Krogt, I. Grigoriev, A. Akhmanova, H. Rehmann and J. de Rooij, *J. Cell Biol.*, 2012, **196**, 641–652.
- 41 Q. Le Duc, Q. Shi, I. Blonk, A. Sonnenberg, N. Wang, D. Leckband and J. De Rooij, *J. Cell Biol.*, 2010, **189**, 1107–1115.
- 42 R. C. Andresen Eguiluz, K. B. Kaylan, G. H. Underhill and D. E. Leckband, *Biomaterials*, 2017, **140**, 45–47.
- 43 E. Dejana, M. G. Lampugnani, M. Giorgi, M. Gaboli and P. C. Marchisio, *Blood*, 1990, **75**, 1509–17.
- 44 Y.-F. Cheng, R. I. Clyman, J. Enenstein, N. Waleh, R. Pytela and R. H. Kramer, *Exp. Cell Res.*, 1991, **194**, 69–77.
- 45 M. H. Wu, E. Ustinova and H. J. Granger, *J. Physiol.*, 2001, **532**, 785–791.
- 46 J. M. Goffin, P. Pittet, G. Csucs, J. W. Lussi, J. J. Meister and B. Hinz, *J. Cell Biol.*, 2006, **172**, 259–268.
- 47 D. Riveline, E. Zamir, N. Q. Balaban, U. S. Schwarz, T. Ishizaki, S. Narumiya, Z. Kam, B. Geiger and A. D. Bershadsky, *J. Cell Biol.*, 2001, **153**, 1175–1185.
- 48 J. Millán, R. J. Cain, N. Reglero-Real, C. Bigarella, B. Marcos-Ramiro, L. Fernandez-Martin, I. Correas and A. J. Ridley, *BMC Biol.*, 2010, **8**, 11.
- 49 N. Zebda, O. Dubrovskiy and K. G. Birukov, *Microvasc. Res.*, 2012, **83**, 71–81.
- 50 K. M. Arnold, Z. M. Goeckeler and R. B. Wysolmerski, *Microcirculation*, 2013, **20**, 637–649.
- 51 Z. M. Goeckeler, P. C. Bridgman and R. B. Wysolmerski, *Am J Physiol Cell Physiol*, 2008, **295**, C994-1006.
- 52 J. R. Guyton and K. F. Klemp, *Am. J. Pathol.*, 1993, **143**, 1444–1457.
- 53 H. C. Stary, A. Chandler, S. Glagov, J. R. Guyton, W. Insull, M. J. Rosenfeld, S. Schaffer, C. Schwartz, W. Wagner and R. Wissler, *Circulation*, 1994, **89**, 2462–2478.
- 54 R. Ross, *N. Engl. J. Med.*, 1999, **340**, 115–126.
- 55 J. Hughes, R. J. Johnson, A. Mooney, C. Hugo, K. Gordon and J. Savill, *Am. J. Pathol.*, 1997, **150**, 223–234.
- 56 C. D. Buckley, E. A. Ross, H. M. McGettrick, C. E. Osborne, O. Haworth, C. Schmutz, P. C. W. Stone, M. Salmon, N. M. Matharu, R. K. Vohra, G. B. Nash and G. E. Rainger, *J. Leukoc. Biol.*, 2006, **79**, 303–311.

- 57 Y. Hirano, M. Aziz and P. Wang, *Biol. Chem.*, 2016, **397**, 497–506.
- 58 K. J. Moore, F. J. Sheedy and E. A. Fisher, *Nat. Rev. Immunol.*, 2013, **13**, 709–721.
- 59 C. A. Reinhart-King, M. Dembo and D. A. Hammer, *Biophys. J.*, 2008, **95**, 6044–6051.
- 60 A. K. Harris, P. Wild and D. Stopak, *Science (80-. )*, 1980, **208**, 177–179.
- 61 R. F. M. van Oers, E. G. Rens, D. J. LaValley, C. A. Reinhart-King and R. M. H. Merks, *PLoS Comput. Biol.*, 2014, **10**, e1003774.
- 62 Y. A. Komarova, K. Kruse, D. Mehta and A. B. Malik, *Circ. Res.*, 2017, **120**, 179–206.
- 63 H. N. Hayenga, A. Trache, J. Trzeciakowski and J. D. Humphrey, *J. Vasc. Res.*, 2011, **48**, 495–504.
- 64 P. Tracqui, A. Broisat, J. Toczek, N. Mesnier, J. Ohayon and L. Riou, *J. Struct. Biol.*, 2011, **174**, 115–123.



40x20mm (300 x 300 DPI)